Research article

Histone lactylation-related genes correlate with the molecular patterns and functions of cancer-associated fibroblasts and have significant clinical implications in clear cell renal cell carcinoma

Weiyu Kong [a,b,1], Jiaxin He [c,1], Qinyao Zhou [c,1], Xin Zhou [c,1], Xiyi Wei [b], Yonglin Yang [d], Yiwen Mei [b], Shuai Wang [b], Xi Zhang [b], Bing Yao [c], Yulin Yue [e,****], Jiali Xu [f,**], Minjun Jiang [a,***], Chen Xu [a,*]

[a] Department of Urology, Suzhou Ninth People's Hospital, Soochow University, Suzhou, 215000, China
[b] Department of Urology, The First Affiliated Hospital of Nanjing Medical University, Nanjing, 210029, China
[c] National Experimental Teaching Center of Basic Medical Science, School of Basic Medical Sciences, Nanjing Medical University, Nanjing, China
[d] The Affiliated Taizhou People's Hospital of Nanjing Medical University, Taizhou School of Clinical Medicine, Nanjing Medical University, Taizhou, China
[e] Department of Clinical Laboratory, Children's Hospital of Nanjing Medical University, Nanjing, China
[f] Department of Oncology, The First Affiliated Hospital of Nanjing Medical University, Nanjing, China

A R T I C L E   I N F O

A B S T R A C T

Recent research emphasised the indispensable role of histone lactylation in the activation of hepatic stellate cells. The VHL mutation is extremely common in clear cell renal cell carcinoma, which normally causes a metabolic shift in cancer cells and increases lactate production, eventually creating a lactate-enriched tumour microenvironment. Cancer-associated fibroblasts (CAFs) promote tumour progression, which is also vital in clear cell renal cell carcinoma. Therefore, this study investigated histone lactylation in CAFs and its impact on patient survival. Multiomics technology was employed to determine the role of histone lactylation-related genes in the evolution of CAFs which correlated with the function and molecular signatures of CAFs. The results suggested that TIMP1 was the hub gene of histone lactylation-related genes in clear cell renal cell carcinoma.

1. Introduction

In 2022, kidney and renal pelvis cancer comprised 5 per cent of estimated new cases, ranking sixth among all cancer types [1]. Clear cell renal cell carcinoma (ccRCC) is the most common type of renal cell carcinoma, accounting for more than 70 per cent of RCC. VHL mutations occur in most ccRCC cases and induce cancer cells to undergo metabolic reprogramming to an aerobic glycolysis phenotype

---

* Corresponding author.
** Corresponding author.
*** Corresponding author.
**** Corresponding author.
E-mail addresses: yueyulin@njmu.edu.cn (Y. Yue), xujiali@jsph.org.cn (J. Xu), 13606258811@189.cn (M. Jiang), chenadoc@126.com (C. Xu).
[1] Weiyu Kong, Jiaxin He, Qinyao Zhou and Xin Zhou contributed equally to this work.

[2,3], generating a lactate-enriched tumour microenvironment (TME).

A recent study disclosed the significance of histone lactylation in hepatic stellate cell activation and identified 1126 H3K18la-marked genes [4]. In addition, Yang et al. elucidated that the coupling of inactive VHL and histone lactylation induced platelet-derived growth factor receptor β (PDGFRβ)promoting tumour progression, and inhibition of histone lactylation and PDGFRβ impeded tumour growth and improved therapeutic efficacy in ccRCC [5]. Since the concept of histone lactylation was proposed [6], its importance has been corroborated in numerous cancer types including ocular melanoma [7], prostate cancer [8], liver cancer [9] and ccRCC [10]. However, few studies have investigated the role of histone lactylation in cancer-associated fibroblasts (CAFs) in ccRCC. Considering their great value in shaping the TME [11,12] and assisting tumour resistance to immunotherapy [13,14], it is necessary to investigate the plasticity of CAFs to histone lactylation.

This study employed multiomic technologies to investigate the significant role of histone lactylation-related genes in the evolution of CAFs. The evolutionary process of CAFs with histone lactylation-related genes was explored using single-cell RNA sequencing (scRNA-seq) data and three stages were defined based on the gene expression trajectories. The distribution modalities and gene expression patterns were explored in different molecular clusters, where common patterns of histone lactylation-related genes were observed in the high myoCAF infiltrated region. Moreover, patients in the TCGA-KIRC cohort were clustered into high and low histone lactylation subgroups with significant differences in clinical status and immune signatures. Finally, TIMP1 was identified as the hub gene, and it alone or together with its receptors had significant value in predicting patient overall survival which was gender-related.

2. Methods

2.1. Data acquisition

The bulk RNA sequencing results and clinical data of TCGA-KIRC (tumour: 541, normal: 72) were downloaded from the Cancer Genome Atlas (TCGA) database (https://www.cancer.gov/tcga) with the E-MTAB-1980 cohort containing 101 ccRCC samples utilised for validation. Notably, the raw count format data of TCGA-KIRC was used for the detection of differentially expressed genes (DEGs), while the transcripts per kilobase million (TPM) format data was utilised for other analyses. For genes with multiple sequencing results, the highest RNA expression was utilised.

The single-cell RNA sequencing (scRNA-seq) data, single-cell Assay for Transposase-Accessible Chromatin using sequencing (scATAC-seq) data and Spatial Transcriptomics (ST) data can be accessed in GSE207493 [15], GSE210042 [10] and GSE175540 [16]. The immunomodulatory genes were generated and revised from previous research [17].

2.2. Differentially expressed gene extraction

The Wilcoxon test and R package *Limma* [18] were used to detect differentially expressed histone lactylation-related genes in tumour and normal tissues, with the criteria set as the absolute logFC greater or equal to 0.2 and a false discovery rate (FDR) lower than 0.05. Random forest was performed using the R package *randomForest* [19], and the uniCox and Least absolute shrinkage and selection operator (LASSO) was based on the R package *glmnet* [20–22].

2.3. Calculation of enrichment scores

Genes used to calculate the histone lactylation score were obtained from the study by Rho et al. [4] which identified 1126 genes marked by H3K18la in the activation of hepatic stellate cells. These gene symbols were transformed to yield 1118 genes with corresponding gene symbols, referred to as the histone lactylation-related gene (HLRG) list, which was used to calculate the histone lactylation score (see Supplemental materials). The normal fibroblast and CAF-related signatures were generated from R package *IOBR* [23] including Normal.Fibroblast, ecm.myCAF, TGFb.myCAF, wound.myCAF, detox.iCAF, IL.iCAF and IFNG.iCAF. The histone lactylation scores and CAF-related signature scores in scRNA-seq and ST data were calculated using *AddModuleScore* based on R package *Seurat* [24–27], while the histone lactylation scores were calculated using Gene Set Variation Analysis (GSVA) in the bulk RNA sequencing data based on the 380 upregulated genes in tumour tissue according to the R package *GSVA* [28]. The estimated CAF-related signature scores in bulk RNA sequencing data were obtained using R package *IOBR* based on the single sample gene set enrichment analysis (ssGSEA) algorithm.

2.4. Survival analysis

The prognostic analysis was implemented using the R packages *survival* and *survminer* [29]. The statistically significant criterion was set as p-value <0.05 and the *surv_cutpoint* was used to calculate the optimal cutoff value. A nomogram was constructed based on the R package *nomogramFormula* which was drawn using *DynNom* [30].

2.5. Correlation analysis

The correlation analysis was conducted using the R package *ggplot2* [31] based on spearman correlation method, and the statistically significant criterion was set as p-value <0.05.

2.6. Processing of the single-cell RNA sequencing data

The R package *Seurat* [24–27] was used to filter out low-quality cells in GSE210038, retaining cells with feature counts <3500 and a percentage of mitochondrial reads <20 %. Then, *FindIntegrationAnchors* (with the reduction parameter set as "rpca") and the *IntegrateData* command were used for data integration and batch effect removal before the *RunPCA* and *RunUMAP* commands were used for dimensionality reduction. The 30 most remarkable principal components and the top 2000 highly variable genes were filtered and clustered using the *FindNeighbors* and *FindClusters* commands with a resolution of 0.8. The canonical marker genes to identify clusters were obtained from the literature. For the re-clustering of MSCs, the resolution parameter was set to 0.1 to avoid excessive distinction.

Notably, for scRNA-seq data of GSE207493, the raw data was first filtered with the following criteria: 1) after clustering, the space between each cell cluster should be distinct; 2) the absolute cell number of ACTA2 positive clusters should be greater than 200; 3) the cell proportion of ACTA2 positive clusters should be greater than 0.07. Finally, 9 of 19 samples were selected with a comparatively sufficient number of MSCs for further study (Fig. S1). The filtering criteria were set as a feature count <7500, a unique molecular identifier (UMI) count ranging from 1500 to 10000 and a percentage of mitochondrial reads <10 %. The integration and dimensionality reduction methods were consistent with GSE210038 and the resolution parameter was set to 0.6.

2.7. Evaluation of tissue distribution preferences

The Ro/e value was calculated in different tissues to evaluate the distribution preferences of each cell type based on the chi-squared test, as previous research had introduced [32]. A Ro/e value greater than 1 represented high infiltration of one cell type. And the Ro/e index was defined to show the cell type preference in a specific tissue (+++: Ro/e > 3; ++: 1 < Ro/e ≤ 3; +: 0.2 ≤ Ro/e ≤ 1; +/−: 0 < Ro/e < 0.2; and −: Ro/e = 0).

2.8. Processing of the ST data

The ST data was processed using Python scanpy 1.9.3 and the top 5000 variable genes with the parameters of *scanpy.pp.neighbors* set to *n_neighbors* equal to 40 and *n_pcs* equal to 40. The clustering results were generated with the Leiden algorithm and exported for further study in R.

2.9. Estimation of cell composition in the ST analyses

The multimodal intersection analysis (MIA) method was used to calculate the composition of cells in distinct clusters [33] (Fig. 3B). The single-cell RNA cluster marker detection was set as a logFC >0.25 and should be expressed in a minimum fraction of 25 % cells in the specific cluster with the *FindAllMarkers* command. The ST cluster marker detection was set as a logFC >0.1 and should be expressed in a minimum fraction of 10 % spots in the specific cluster (see Supplemental materials). With the gene sets extracted from the scRNA-seq and ST, the MIA method performed a hypergeometric test to assess significant enrichment or depletion based on the computed results of the overlapping genes between each pair of cell type-specific and region-specific gene sets. To better visualise the spatial distribution, an enrichment score greater than 20 represented high infiltration of mesangial cells and the highest histone lactylation stage enrichment score represented the overall status of mesangial cells in the specific cell clusters.

2.10. Processing of the single-cell ATAC sequencing data

The processing for single-cell ATAC data was based on the R package *Signac* [34]. The combined peaks were generated using the *reduce* function in the R package *GenomicRanges* to merge the selected 9 single-cell ATAC data [35] and the detailed method for integration can be accessed in the "Merging objects" tutorial of the Signac website (https://stuartlab.org/signac/articles/merging.html). For quality control, the peak region fragments ranged from 2000 to 20000, the percentage of reads in peaks was >15, the nucleosome signal was <4 and a transcription start sites (TSS) enrichment value was >1. The minimum cutoff value for the *FindTopFeatures* function was set to q5 and the second to 30th dims were concluded for the *RunUMAP* and *FindNeighbors* commands. The resolution was set to 0.4 for the identification of cell clusters with the *FindClusters* command. Both RNA values as inferred by the R package *ChIPseeker* [36] and the chromatin accessibility results (Fig. S2) were incorporated to identify the cell types in the scATAC-seq.

2.11. Cell trajectory analysis

The pseudotime of cell trajectory was computed based on the R package *monocle*, version 2.22.0 [37,38]. First, the *differentialGeneTest* command was utilised with an adjusted p-value ≤0.05 as criteria to obtain differentially expressed genes based on re-clustering results and then the genes intersecting the histone lactylation gene list were selected (Fig. 2A–D).

2.12. Gene expression patterns and interaction density of ST analysis

The R package *SpaGene* [39] was used to generate the expression patterns of different ST samples with the nPattern set to 6 and the interaction scores and p-value were obtained using the *SpaGene_LR* command using the Earth mover's distance which was based on the degree distribution of the subnetwork.
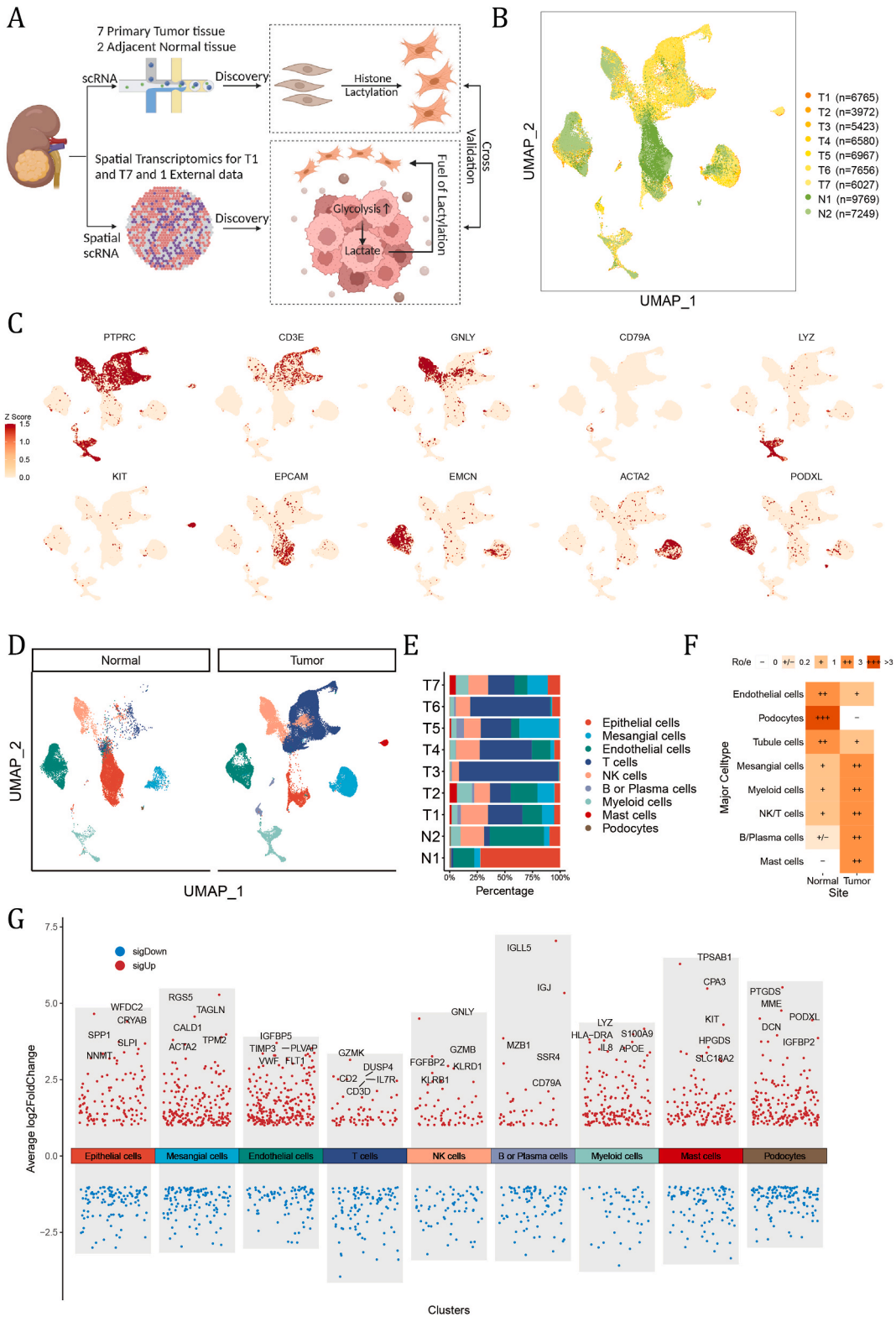
Fig. 1. Single-cell RNA sequencing data analysis. (A) Workflow of discovery, (B) summary of the number of cells in each sample. (C) Canonical cell markers for cell identification. (D) Umap plot showing the annotated cell types from two normal adjacent tissue (left) and seven tumour tissue samples (right). (E) The percentage of annotated major cell types in each sample. (F) Tissue preference of each major type in normal and tumour samples estimated by Ro/e. (G) Expression features of each cell type. (Genes were randomly distributed in the X-axis).
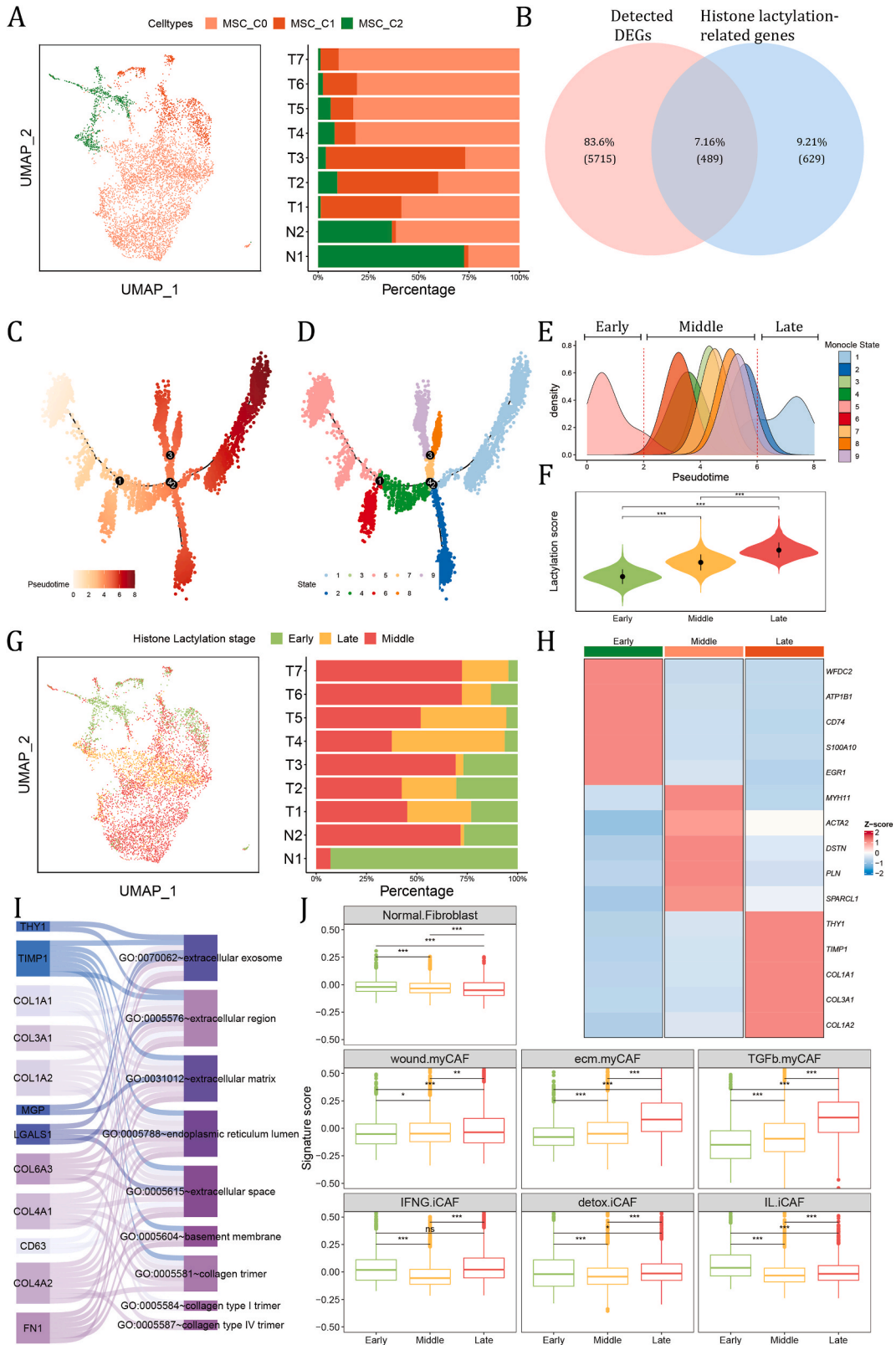
(caption on next page)

Fig. 2. Cell trajectory analysis of mesangial cells (MSC). (A) Umap plot of re-clustered MSCs (left); the proportion of re-clustered MSCs in each sample (right). (B) Venn plot displaying the overlapping genes. (C) Pseudo cell trajectory of MSCs using overlapping genes, (D) cell states determined by the cell branch, (E) density plot showing the distribution of pseudotime in different cell states, and (F) violin plot displaying the lactylation score in the distinct histone lactylation stages (*p ≤ 0.05, **p ≤ 0.01, ***p ≤ 0.001). (G) Umap plot showing the distribution of histone lactylation stages (left); the proportion of histone lactylation stages in each sample (right), (H) heatmap showing the gene signatures of three histone lactylation stages, (I) GO cell component results of top 15 late histone lactylation stage DEGs, and (J) a comparison of the specific markers in the three histone lactylation stages (*p ≤ 0.05, **p ≤ 0.01, ***p ≤ 0.001).

2.13. Estimation of immune cell infiltration and TME

The predicted TME signatures were generated by R package *Estimate* [40] and *IPS*. In *IPS*, the suppresser cells represented the general level of infiltrated myeloid-derived suppressor cells (MDSCs) and regulatory T cells (Tregs), while effector cells included activated CD4 T cells, activated CD8 T cells, effector memory CD4 T cells and effector memory CD8 T cells. The predicted infiltration of immune cells was calculated with the MCPcounter, EPIC, quantiseq and xCell algorithm using the R package *IOBR*.

2.14. Pathway enrichment analysis

The Gene Ontology (GO) and the hallmark gene set enrichment analysis were conducted using the R package *clusterProfiler* [41,42] and gene sets downloaded from the R package *org.Hs.eg.db* and the Molecular Signatures Database (MSigDB) with the aid of R package *msigdbr* [43]. Pathways with a p-value <0.05 and false discovery rate (FDR) < 0.05 were considered significant.

2.15. Random forest analysis

Random forest (RF) analysis was performed using the R package *randomForest* with 80 per cent of the samples randomly included in the training cohort and the remaining 20 per cent in the validation cohort. The *ntree* parameter was set to 100 in the *randomForest* command and the gene importance in the model was calculated using the *importance* command with the *type* parameter set to 2, namely the Gini Impurity method.

2.16. Multiplex immunofluorescence (mIF) assay

CA9, COL1A1 and TIMP1 antibodies were obtained for mIF assay. Briefly, cells were fixed by 4 % PFA, permeabilized via 0.1 % Triton X-100, and cultured with primary antibody. After visualization through secondary antibodies, cell nuclei underwent counterstaining by utilizing DAPI staining. Images were captured using a fluorescence microscope (XSP-63B, Shanghai Optical Instrument Factory).

2.17. Application of R

The expression patterns of ST data were analysed using scanpy in Python and other analyses were conducted utilizing R 4.1.3 and R 4.3.1. Independent t-tests were used to compare continuous variables with a normal distribution for inter-group comparison, while Mann-Whitney U-tests were used to compare continuous variables with a skewed distribution.
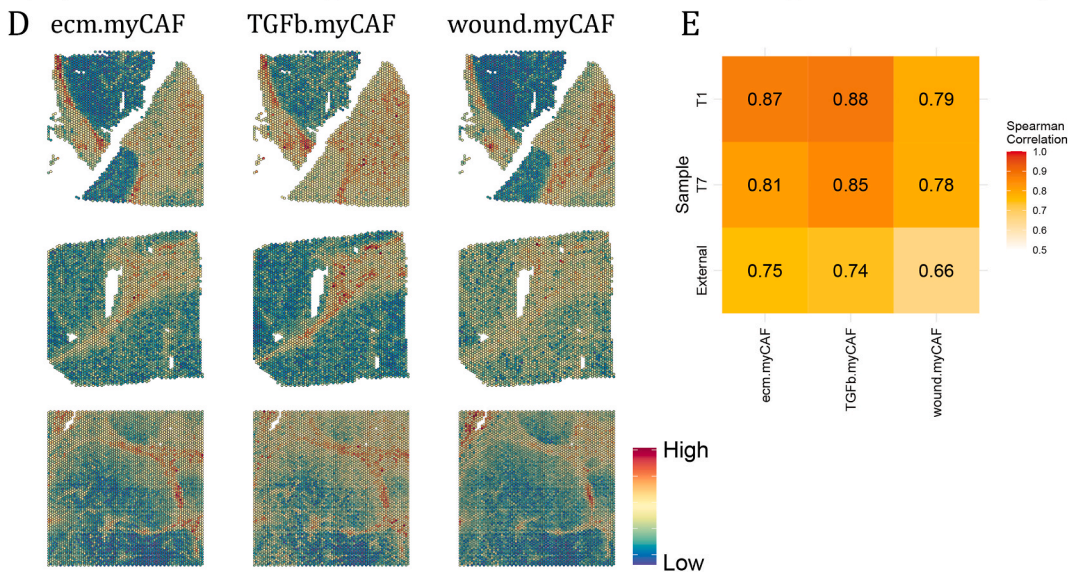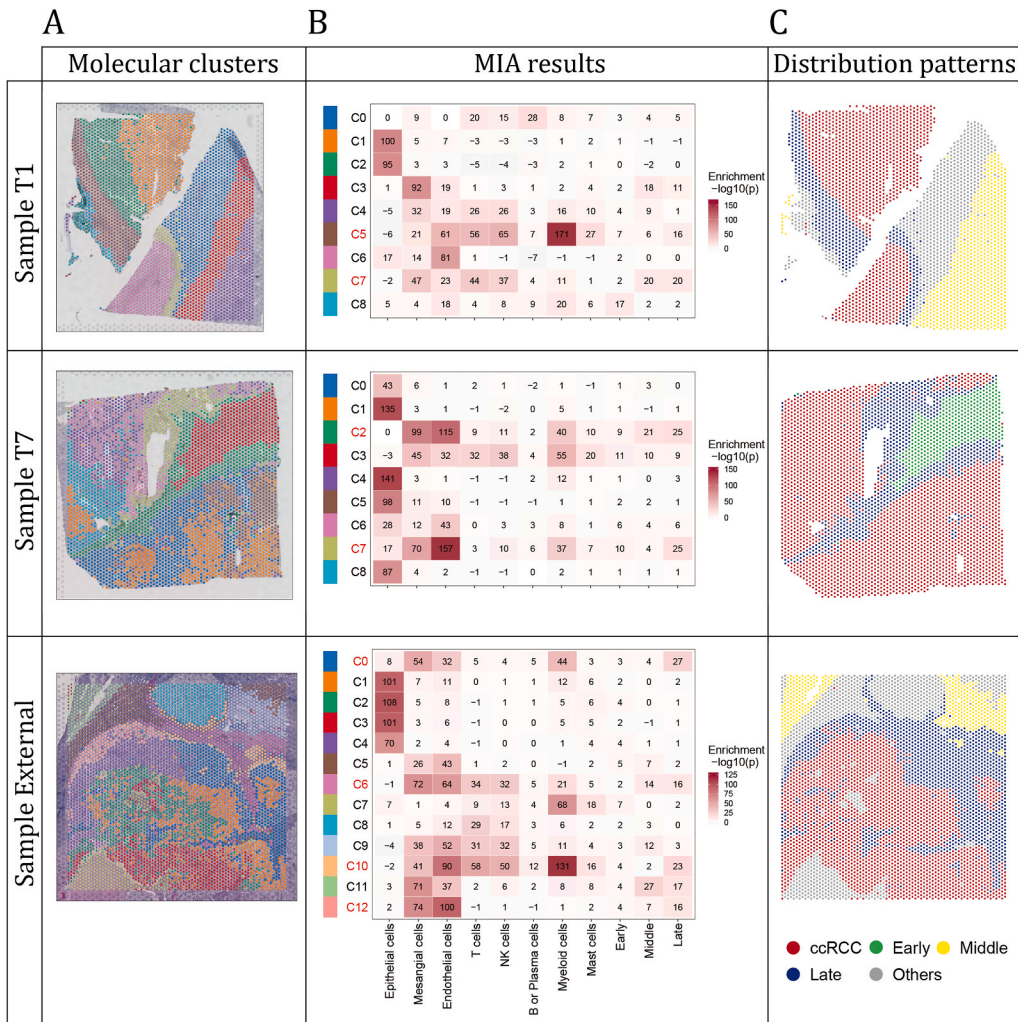
3. Results

3.1. Identification of cell types in the single-cell RNA sequencing data

As shown in Fig. 1A, nine scRNA-seq data were generated including seven primary tumour and two adjacent normal tissues (Fig. 1B), and the paired spatial transcriptomics for T1 and T7 and one external ST data for the discovery of histone lactylation in fibroblasts in ccRCC (see Supplemental materials).
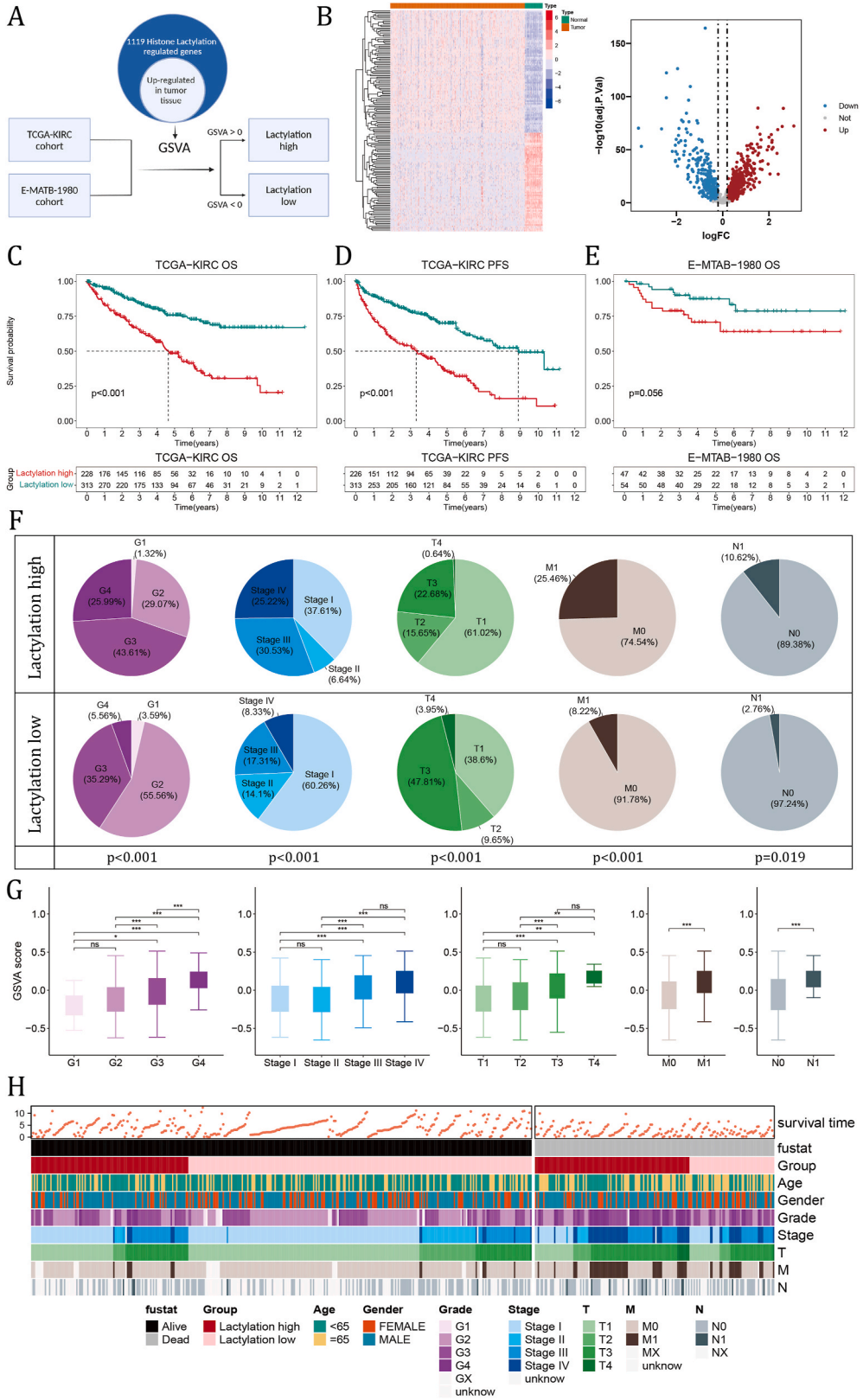
According to the cell markers (Fig. 1C) (PTPRC: immune cells, CD3E: T cells, GNLY: NK cells, CD79A: B or Plasma cells, LYZ: Myeloid cells, KIT: Mast cells, EPCAM: Epithelial cells, EMCN: endothelial cells, ACTA2: Mesangial cells, PODXL: Podocytes), the integrated samples were clustered and annotated into eight cell types (Fig. 1D). The distribution of each major cell type differed among samples (Fig. 1E), and the mesangial cells (referred to as MSCs) occurred in all samples and were slightly more likely to occur in the tumour samples, as was revealed by the ratio of observed to expected cell numbers (Ro/e) (Fig. 1F). The clustering results were validated in Fig. 1G of the gene expression marker of each cell type such as CD79A for B or plasma cells, ACTA2 and RGS5 for mesangial cells.

3.2. Expression of histone lactylation-related genes distinguished the state of MSCs

The mesangial cells were extracted and grouped into three main sub-clusters with cluster 2 MSCs mainly concentrated in the normal sample (Fig. 2A). To elucidate the role of histone lactylation-related genes (HLRGs) in the transformation of MSCs, the differentially expressed genes were identified in the three sub-clusters and compared to the HLRG list, selecting 489 HLRGs to illustrate

Fig. 3. Integrated scRNA-seq and ST revealed the distribution of CAFs in ccRCC. (A) Spatial plot showing the molecular clusters in each sample, (B) the MIA results displaying the spatial distribution of cells in each molecular cluster, (C) spatial plots visualising the distribution patterns based on MIA results. (D) The signature scores in each spot, and (E) Spearman correlation of the late histone lactylation score with three myoCAF signature scores.

Fig. 4. The molecular patterns in the high-CAF infiltrated area. (A) Molecular patterns of three ST samples as defined by SpaGene. (B) Gene expression signatures of different patterns. (C) GO results of the overlapping up-regulated genes in all the selected patterns. (D) Venn plot showing the intersecting genes of the selected patterns in three ST samples and the HLRG list. (E) Heatmap showing the known ligand-receptor interacting score (*p ≤ 0.05, **p ≤ 0.01, ***p ≤ 0.001).

(caption on next page)

Fig. 5. Histone lactylation has clinical implications in ccRCC. (A) Workflow of discovery. (B) Heatmap displaying the expression signatures in tumour and normal tissues (left), volcano plot displaying the distribution of differentially expressed genes (right). (C–E) Kaplan-Meier plots of TCGA-KIRC and E-MTAB-1980 overall survival (OS) and progression-free survival (PFS). (F) The proportion of patients with distinct histologic tumour grades, clinical stages and TNM stages in the TCGA-KIRC cohort, (G) the differences in lactylation score in detailed histologic tumour grades, clinical stages and TNM stages (*$p \leq 0.05$, **$p \leq 0.01$, ***$p \leq 0.001$), and (H) a heatmap summarising the general clinical status of patients in the TCGA-KIRC cohort.

the trajectory of MSCs (Fig. 2B) with a total of eight trajectory states generated (Fig. 2C and D). As the pseudotime increased, these cell states displayed three main modalities defined as the early, middle and late histone lactylation stage (HLS) based on the calculated pseudotime, with 25 per cent and 75 per cent of pseudotime as the dividing line (Fig. 2E). The histone lactylation score was calculated, showing a steady increase in the lactylation score as the histone lactylation stage advanced (Fig. 2F).

As illustrated in Fig. 2G, cells in the early HLS mostly overlapped with cluster 2 MSCs, while cells in the late stage were enriched in the tumour tissue. Notably, considering the differentially expressed genes, around 25 per cent of these early-stage MSCs had elevated expression of antigen-presenting markers including CD74 and HLA-DRA referred to as antigen-presenting CAFs (apCAFs), while in the late-stage cells, gene signatures such as the markers for myofibroblastic CAFs (myoCAFs) COL1A1, COL3A1 and COL1A2 were dominant (Fig. 2H and Supplemental materials). As further validation, these elevated genes in the late-stage MSCs were enriched in GO cell component terms related to the extracellular space and extracellular matrix (Fig. 2I). As shown in Fig. 2J, the signature score for normal fibroblasts decreased steadily as the HLS increased and three myoCAF signature scores increased stepwise in advanced HLS, indicating their myoCAF-resembling signatures in these late HLS MSCs.

3.3. Spatial transcriptomics data validated the infiltration of CAFs and their distribution patterns

The ST samples T1 and T7 were paired with the scRNA-seq data, and the external sample was generated from GSE175540 for validation. Based on the gene expression patterns, spots in the ST data were divided into distinct molecular clusters (Fig. 3A) and the MIA method [44] was applied to estimate the composition of each cell cluster with the scRNA-seq annotation results from seven tumour samples with the differentially expressed genes among HLSs as the reference data. Regions with both high mesangial cell and late-stage enrichment scores were located close to cancer cell regions, while regions with high early- and middle-stage enrichment scores were rather distant from the tumour tissue, indicating the spatial dependency of myoCAF and cancer cells (Fig. 3B and C). As illustrated in Fig. 3D, spots with high myoCAF-related signature scores were mostly located in the late-stage MSC-infiltrated region, with the histone lactylation score correlating with the myoCAF signature scores (Fig. 3E). These results suggest the close spatial distribution of CAFs, especially myoCAFs, with cancer cells to promote tumour progression.

3.4. The high CAF infiltrated region had specific gene expression patterns

To elucidate the possible role of CAFs in promoting cancer, the molecular signatures and their cell-cell communication patterns were evaluated. Each sample was divided into six patterns to identify the high CAF-infiltrated patterns by referring to the MIA and gene signature clustering results (Fig. 4A and B). The selected patterns were composed mostly of clusters with high middle-stage and late-stage enrichment scores (Fig. 3C). The GO results of commonly up-regulated genes in the selected patterns indicated similar functioning modalities, especially in sample T1 and the external sample (Fig. 4C). Combined with the MIA results, patterns 3, 4 and 6 in sample T1 comprised mostly of molecular clusters 3, 4, 5 and 7, clusters 4, 5 and 7 also had high NK cell and T cell infiltration and cluster 5 had an extremely high enrichment score of myeloid cells. Similarly, clusters 6, 9 and 10 in the external sample had high infiltration of NK cells and T cells and clusters 0, 7 and 10 had an abundance of infiltrated myeloid cells. The elevated genes in sample T7 were enriched in extracellular matrix formation, with pattern 3 contributing most to these results (Fig. 4C). Based on the MIA results, patterns 3 and 4 in sample T7 mainly included clusters 2, 3 and 7, with clusters 2 and 7 containing mostly late-stage MSCs and myeloid cells, while cluster 3 also had high NK cell and T cell infiltration. As shown in the heatmap, the expression of immune-related gene signatures such as CD74 and HLA-DRA was mildly elevated. The overall intersection of gene signatures, despite different relative expression levels, suggested the common distribution of CAFs, cancer cells and immune cells, providing evidence for the common TME in ccRCC. There were nine intersecting genes of samples T1, T7, the external sample and the HLRG list, five of which had known receptors (Fig. 4D). The estimated interaction score is shown in Fig. 4E indicating their indispensable role in the TME.

3.5. The overall histone lactylation level in ccRCC had robust clinical significance

The histone lactylation score was calculated using GSVA with a GSVA score >0 considered as high lactylation and then the samples in the TCGA-KIRC and E-MTAB-1980 cohorts were divided into high and low lactylation subgroups for further analyses (Fig. 5A and B). The high lactylation subgroups of TCGA-KIRC cohort had significantly poorer overall survival (OS) and progression-free survival (PFS), while the high lactylation subgroup represented relatively worse OS in the E-MTAB-1980 cohort (p = 0.056) (Fig. 5C–E). Furthermore, the high lactylation subgroup in the TCGA-KIRC cohort had a significantly larger proportion of advanced ccRCC samples including higher histologic tumour grading, clinical staging and detailed TNM stages (Fig. 5F). The lactylation score increased steadily with tumour progression, which was especially significant between G1/G2 and G3/G4, Stage I/II and Stage III/IV, and T1/T2 and T3/T4, and was significantly higher in M1 and N1 patients (Fig. 5G). The overall status of samples in the TCGA-KIRC cohort was summarised
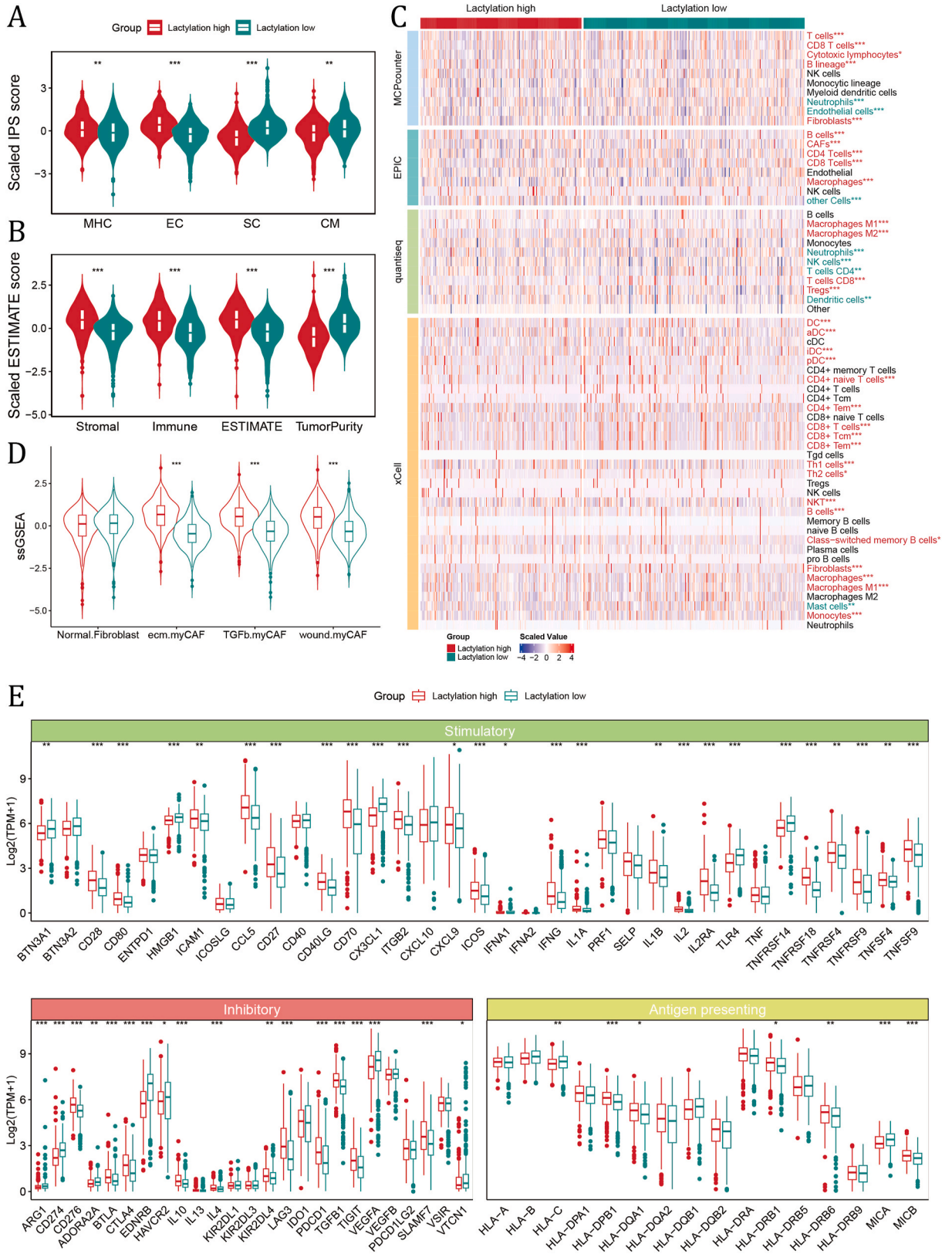
(caption on next page)

Fig. 6. A comparison of the immune landscape in the high and low lactylation subgroups in the TCGA-KIRC cohort. (A) Immune signatures calculated by the IPS algorithm. MHC, MHC molecules; EC, effector cells; SC, suppressor cells; CM, checkpoint molecules. (B) Immune signatures calculated by the ESTIMATE algorithm. (C) Deconvolution results of immune cells based on four algorithms of the lactylation subgroups. Cells in red represent a higher level of estimated infiltration in the high lactylation subgroup and cells in green represent a higher level in the low lactylation subgroup (*p ≤ 0.05, **p ≤ 0.01, ***p ≤ 0.001). (D) Violin plot showing the differences in ssGSEA results based on some known normal fibroblast and CAF-related gene sets, and (E) in immune-related molecules between the high and low lactylation subgroups.

in Fig. 5H, indicating that the lactylation score is closely associated with patient outcomes and survival, where an increased lactylation score correlated with poorer clinical status.

3.6. The high lactylation subgroup had more infiltrated immune cells and fibroblasts

Considering the great heterogeneity in TME and the co-localisation of CAFs with immune cells, the immune landscape of samples in the lactylation subgroups was evaluated based on numerous immunity-related algorithms. The high lactylation subgroup had significantly more MHC molecules and effector cells (EC) but fewer suppressor cells (SC) and checkpoint molecules (CM) (Fig. 6A), as well as higher immune scores (Fig. 6B). There were also significantly more T cells, especially CD8 T cells, macrophages and fibroblasts, as well as significantly higher myoCAF signature scores (Fig. 6C and D). Additionally, there were more stimulatory molecules and antigen-presenting molecules, as well as inhibitory molecules such as LAG3, PDCD1, TIGIT and CD276 in the high lactylation subgroup (Fig. 6E).

3.7. TIMP1 was the hub gene in the HLRGs in CAFs and predicted patient prognosis

The gene most contributing to histone lactylation in ccRCC (Fig. 7A) was identified as TIMP1 (Fig. 7B). TIMP1 expression was validated in samples T1, T7 and the external sample with ST data, showing that it was particularly concentrated in the high myoCAF infiltrated regions (Fig. 7C–E). And the multiplex immunofluorescence(mIF) results of ccRCC validated that TIMP1 co-localized with COL1A1, which was a representing marker of late-stage CAFs and myoCAFs, indicating that myoCAFs were the main source of TIMP1 (Fig. 7F). Moreover, the relatively high chromatin accessibility of TIMP1 was demonstrated (Fig. 7G), providing evidence for the correlation between gene expression and histone lactylation from another perspective (Figs. S1 and S2).

A nomogram was constructed for the prediction of patient prognosis, where TIMP1, M stage and age were the most dominant factors (Fig. 7H). The calibration plot showed that the nomogram accurately predicted long-term survival, especially 5-year survival status (Fig. 7I–K).

TIMP1 is associated with inflammatory diseases, acts as a potent cytokine, and binds to several cell-surface receptors [45] including CD63, CD74, CD44, LRP1, and CD82. CD63 was highly expressed in the tumour tissue and co-localised with CD74 along the cancer cell border. CD44 and LRP1 were expressed in the high CAF-infiltrated regions, with relatively low expression of CD82 (Fig. 8A–C). The expression of TIMP1 and its receptors had robust clinical implications, with patients with low TIMP1 expression generally having longer overall survival (Fig. 8D). Patients with a combined high expression of TIMP1 with CD44, CD82 had the worst clinical outcomes among other groups. For CD63, it distinguished the differences in OS in both TIMP1 high and TIMP1 low subgroups, where higher expression of CD63 represented better survival (Fig. 8E–I).

Considering the position of the TIMP1 gene on the X chromosome, TIMP1 was significantly more expressed in males compared to females in both the TCGA-KIRC and E-MTAB-1980 cohorts (Fig. 9A and B), and the CAFs in the late histone lactylation stage were more enriched in the male samples, as was revealed by higher Ro/e value in male compared with female (Fig. 9C). Moreover, the low TIMP1 subgroup had significantly longer OS also in the E-MTAB-1980 cohort (Fig. 9D). Female patients with high TIMP1 levels had the worst prognosis (Fig. 9E), with high TIMP1 levels reflecting poorer overall survival in both female and male patients in the TCGA-KIRC cohort (Fig. 9F and G). In the E-MTAB-1980 cohort, male patients with high TIMP1 expression had poor OS (Fig. 9H), and the prognostic value of TIMP1 with the best cutoff value was only significant in males possibly due to the relatively small number of female patients (Fig. 9I and J).

4. Discussion

Metabolic reprogramming is a common signature in ccRCC [46], particularly glycolysis. VHL mutational loss or inactivation normally induces the accumulation of hypoxia-inducible factor (HIF), leading to lactate production in the TME [47,48]. HIF-1α is also the dominant glycolysis regulator [49]. Previous studies had mainly focused on the immune regulating function of lactate, a vital part of the establishment of the tumour immunosuppressive microenvironment [50–52]. Recently, lactate has been shown to be an important substrate in histone lactylation [6,53]. Rho et al. elucidated the indispensable role of histone lactylation in the activation of hepatic stellate cells and in promoting the secretory phenotype [4]. In this study, we utilised the HLRGs to investigate the evolution of CAFs, revealing the close relationship between HLRG expression and CAF molecular signatures and possible functioning modalities.

Intra-tumoral CAFs are heterogeneous, thus impacting clinical outcomes and therapeutic effects [54]. Three histone lactylation states of MSCs were defined, namely the early, middle and late HLSs. Notably, the early HLS correlated with multiple immune-related genes which were also markers for apCAFs, indicating their role in the anti-tumoral response. The late HLS of MSCs were considered myoCAFs due to their enormous potential in organising the extracellular matrix and correlation with myoCAF signatures.
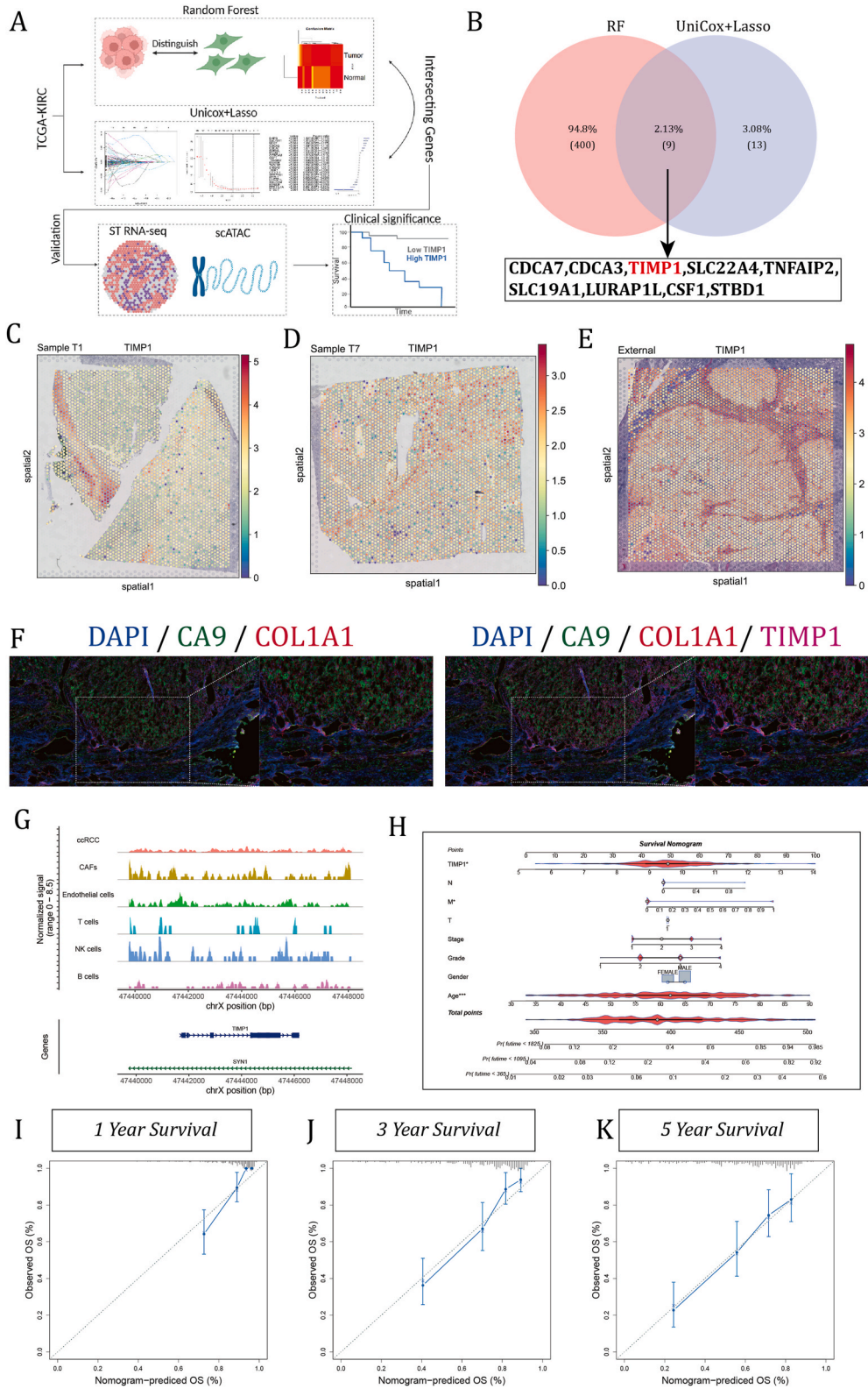
(caption on next page)

Fig. 7. TIMP1 is the hub gene in the HLRGs. (A) Workflow of discovery, (B) the intersection of random forest (RF) results, the uniCox and the Least absolute shrinkage and selection operator (LASSO) results included nine genes ordered by decreasing RF importance. (C–E) Feature plot displayed TIMP1 expression in samples T1, T7 and the external sample. (F) Multiplex immunofluorescence(mIF) results of ccRCC, stained with DAPI (blue), anti-CA9 (green), COL1A1 (red), and TIMP1 (pink) antibodies. Large image taken at $10 \times$ magnification (scale bar = 200 μm). (G) TIMP1 chromatin accessibility results. (H) Survival nomogram established using clinical data and the TPM of gene TIMP1, and (I–K) Calibration plot of 1-year, 3-year and 5-year survival respectively.

The myoCAFs co-localised with immune cells including NK cells, T cells and myeloid cells in the tumour-bordering regions and the highly expressed genes in these areas were associated with T cell activation and mononuclear cell differentiation in sample T1 and the external sample. Nine HLRGs including COL1A1, COL1A2, COL4A2 and COL5A1 were vital in extracellular matrix organisation, demonstrating the significant role of histone lactylation in depicting the spatial distribution of CAFs. With its great potential in remodelling the extracellular matrix around tumour cells, these myoCAFs shaped an immune cell-exclusive TME, leading to immune escape in ccRCC.

In addition, histone lactylation is associated with clinical outcomes, with patients in the high lactylation subgroup more likely to have worse clinical outcomes. The high lactylation subgroup also contained a significantly higher proportion of patients with advanced histologic grades, clinical stages and TNM stages, with an increasing lactylation level with tumour progression. Though with higher estimated infiltration of immune effector cells in the high lactylation subgroup, the distributional and functional characterizations of myoCAF concluded from ST analyses may finally lead to the anergy of immune cells. These results suggest that histone lactylation influences tumour progression. Indeed, histone lactylation in cancer cells also engenders tumour malignancies, promoting cancer proliferation and metastasis in hepatocellular carcinoma [55] and histone lactylation induced YTHDF2 expression leads to tumour initiation in ocular melanoma [7]. Therefore, the perturbation of histone lactylation could directly influence cancer cells and clinical outcomes. And our study extended the significances of histone lactylation in myoCAFs in ccRCC.

TIMP1 was identified as the most vital histone lactylation-regulated gene in ccRCC. TIMP1 was expressed mostly in myoCAFs and had relatively higher chromatin accessibility among other cells. TIMP1 over-expression induced a more proliferative, migrative and invasive RCC cell phenotype [56] and the secretion of TIMP1 by fibroblasts could bind CD63 in cancer cells and induce cancer cell proliferation and invasiveness in lung adenocarcinoma [57]. The co-localisation of TIMP1 and its receptors in both intra-tumoral areas and tumour-neighbouring regions suggests the intricate functions of TIMP1 in ccRCC, thus inhibition of histone lactylation or TIMP1 in the TME may represent a possible therapeutic opportunity. The established nomogram to calculate the clinical significance of TIMP1 in ccRCC had a robust predicting value, especially for 5-year survival.

The present study also revealed that males tended to have higher TIMP1 expression than female patients. Moreover, female patients in the TCGA-KIRC cohort with high TIMP1 levels exhibited poorer survival status with a shorter OS. Although this was not fully verified in the E-MTAB-1980 cohort possibly due to insufficient female patients, a low TIMP1 level was consistent with a longer OS.

In conclusion, this study extends the knowledge regarding lactate and histone lactylation in ccRCC, highlighting the important role of myoCAF-derived TIMP1 in ccRCC which warrants further research. Based on ST data and mIF, we explore the distribution patterns of myoCAFs in ccRCC and emphasize their correlation with histone lactylation.

This study has its limitations, more samples should be concluded and experimental validation is needed. Due to the inherent limitations with current ST technology, we fail to explore the RNA expression in a single-cell resolution. Moreover, the prognostic model requires external datasets to comprehensively assess its accuracy.

Ethics and consent

The ccRCC human tissue was gathered in the Suzhou Ninth People's Hospital with ccRCC. Written informed consent was obtained from patients. Human experiments conducted in this study were approved by the ethics committee of the Suzhou Ninth People's Hospital (KYLW2024-024-01).

Data availability statement

All data generated or analysed during this study are included either in this article or in the supplementary information files. The datasets generated during and/or analysed during the current study are available from the corresponding author on reasonable request.

CRediT authorship contribution statement

Weiyu Kong: Writing – review & editing, Writing – original draft, Visualization, Software, Methodology, Investigation, Formal analysis, Data curation, Conceptualization. **Jiaxin He:** Writing – review & editing, Writing – original draft, Visualization, Data curation. **Qinyao Zhou:** Validation, Methodology, Data curation. **Xin Zhou:** Writing – review & editing, Writing – original draft, Data
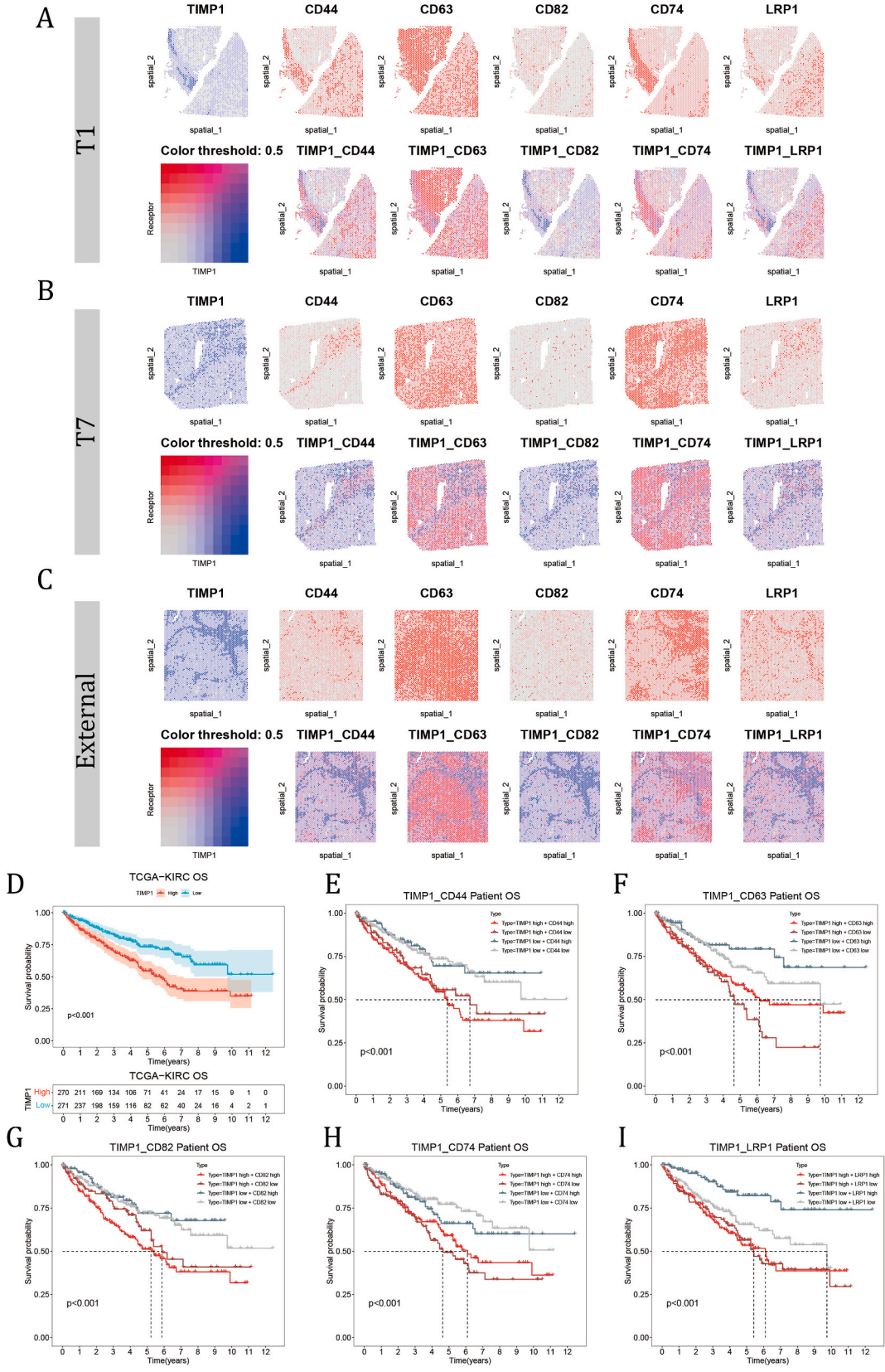
(caption on next page)

Fig. 8. Discovery of the expression patterns of TIMP1 and its receptors in ST data and their clinical significances. (A–C) The expression patterns of TIMP1 and its receptors, and (D–I) KM plots showing the clinical significance of TIMP1 alone and TIMP1 together with its receptors.
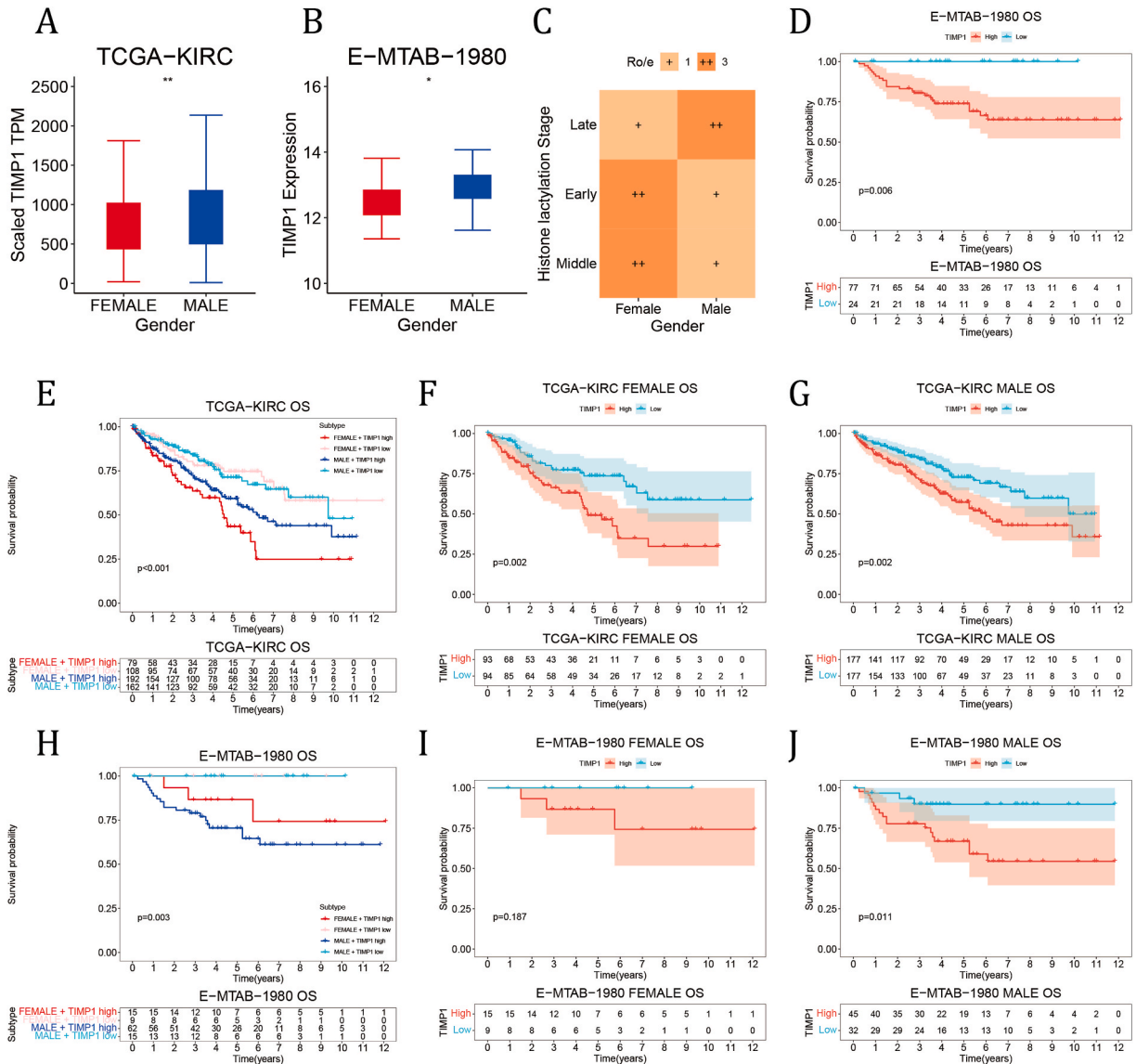

Fig. 9. Comparison of the expression and prognostic value of TIMP1 in male and female ccRCC patients. (A, B) Box plot showing the elevated TIMP1 expression in males compared to females (*p ≤ 0.05, **p ≤ 0.01, ***p ≤ 0.001), (C) Tissue preference of different stages of CAFs in Female and Male samples estimated by Ro/e. (D) KM plot illustrating the prognostic value of TIMP1 in the E-MTAB-1980 cohort, (E–J) KM plot showing the prognostic value of TIMP1 in males and females in the TCGA-KIRC (E–G) and the E-MTAB-1980 cohorts (H–J).

curation. **Xiyi Wei:** Writing – review & editing, Writing – original draft, Visualization, Methodology, Formal analysis, Data curation. **Yonglin Yang:** Writing – review & editing, Writing – original draft, Data curation. **Yiwen Mei:** Writing – review & editing, Writing – original draft, Data curation. **Shuai Wang:** Writing – review & editing, Writing – original draft, Supervision, Resources. **Xi Zhang:** Writing – review & editing, Writing – original draft, Supervision, Resources. **Bing Yao:** Writing – review & editing, Writing – original draft, Methodology, Data curation. **Yulin Yue:** Writing – review & editing, Writing – original draft, Supervision, Methodology, Investigation. **Jiali Xu:** Validation, Methodology, Data curation. **Minjun Jiang:** Writing – review & editing, Methodology, Formal analysis, Data curation. **Chen Xu:** Writing – review & editing, Methodology, Investigation, Data curation.

Declaration of competing interest

The authors declare that they have no known competing financial interests or personal relationships that could have appeared to influence the work reported in this paper.

Appendix A. Supplementary data

Supplementary data to this article can be found online at https://doi.org/10.1016/j.heliyon.2024.e33554.

Abbreviations

CAFs	Cancer associated fibroblasts
ccRCC	Clear cell renal cell carcinoma
TME	Tumuor microenvironment
PDGFRβ	Platelet-derived growth factor receptor β
DEG	Differentially expressed gene
scRNA-seq	Single-cell RNA sequencing
scATAC-seq	Single-cell Assay for Transposase-Accessible Chromatin using sequencing
ST	Spatial transcriptomics
TCGA	The Cancer Genome Atlas
FDR	False discovery rate
HLRG	Histone lactylation related gene
GSVA	Gene Set Variation Analysis
ssGSEA	Single sample gene set enrichment analysis
MIA	Multimodal intersection analysis
TSS	Transcription start sites
MDSC	Myeloid-derived suppressor cells
Tregs	Regulatory T cells
LASSO	Least absolute shrinkage and selection operator
RF	Random forest
GO	Gene Ontology
MSigDB	Molecular Signatures Database
Ro/e	Ratio of observed to expected cell numbers
mIF	Multiplex immunofluorescence
HLS	Histone lactylation stage
apCAF	Antigen-presenting CAF
myoCAF/myCAF	Myofibroblastic CAF
iCAF	Inflammatory CAF
OS	Overall survival
PFS	Progression free survival
MHC	MHC molecules
EC	Effector cells
SC	Suppressor cells
CM	Checkpoint molecules
HIF	Hypoxia-inducible factor

References

[1] R.L. Siegel, K.D. Miller, H.E. Fuchs, A. Jemal, Cancer statistics, 2022, CA A Cancer J. Clin. 72 (1) (2022) 7–33.

[2] L. Gossage, T. Eisen, E.R. Maher, VHL, the story of a tumour suppressor gene, Nat. Rev. Cancer 15 (1) (2015) 55–64.

[3] J.R. Gnarra, K. Tory, Y. Weng, L. Schmidt, M.H. Wei, H. Li, F. Latif, S. Liu, F. Chen, F.M. Duh, et al., Mutations of the VHL tumour suppressor gene in renal carcinoma, Nat. Genet. 7 (1) (1994) 85–90.

[4] H. Rho, A.R. Terry, C. Chronis, N. Hay, Hexokinase 2-mediated gene expression via histone lactylation is required for hepatic stellate cell activation and liver fibrosis, Cell Metabol. 35 (8) (2023) 1406–1423.e1408.

[5] J. Yang, L. Luo, C. Zhao, X. Li, Z. Wang, Z. Zeng, X. Yang, X. Zheng, H. Jie, L. Kang, et al., A positive feedback loop between inactive VHL-triggered histone lactylation and PDGFRβ signaling drives clear cell renal cell carcinoma progression, Int. J. Biol. Sci. 18 (8) (2022) 3470–3483.

[6] D. Zhang, Z. Tang, H. Huang, G. Zhou, C. Cui, Y. Weng, W. Liu, S. Kim, S. Lee, M. Perez-Neut, et al., Metabolic regulation of gene expression by histone lactylation, Nature 574 (7779) (2019) 575–580.

[7] J. Yu, P. Chai, M. Xie, S. Ge, J. Ruan, X. Fan, R. Jia, Histone lactylation drives oncogenesis by facilitating m(6)A reader protein YTHDF2 expression in ocular melanoma, Genome Biol. 22 (1) (2021) 85.

[8] Y. He, Z. Ji, Y. Gong, L. Fan, P. Xu, X. Chen, J. Miao, K. Zhang, W. Zhang, P. Ma, et al., Numb/Parkin-directed mitochondrial fitness governs cancer cell fate via metabolic regulation of histone lactylation, Cell Rep. 42 (2) (2023) 112033.

[9] L. Pan, F. Feng, J. Wu, S. Fan, J. Han, S. Wang, L. Yang, W. Liu, C. Wang, K. Xu, Demethylzeylasteral targets lactate by inhibiting histone lactylation to suppress the tumorigenicity of liver cancer stem cells, Pharmacol. Res. 181 (2022) 106270.

[10] G. Davidson, A. Helleux, Y.A. Vano, V. Lindner, A. Fattori, M. Cerciat, R.T. Elaidi, V. Verkarre, C.M. Sun, C. Chevreau, et al., Mesenchymal-like tumor cells and myofibroblastic cancer-associated fibroblasts are associated with progression and immunotherapy response of clear cell renal cell carcinoma, Cancer Res. 83 (17) (2023) 2952–2969.

[11] M. Desbois, Y. Wang, Cancer-associated fibroblasts: key players in shaping the tumor immune microenvironment, Immunol. Rev. 302 (1) (2021) 241–258.

[12] Z. Peng, M. Ye, H. Ding, Z. Feng, K. Hu, Spatial transcriptomics atlas reveals the crosstalk between cancer-associated fibroblasts and tumor microenvironment components in colorectal cancer, J. Transl. Med. 20 (1) (2022) 302.

[13] R.L. Barrett, E. Puré, Cancer-associated fibroblasts and their influence on tumor immunity and immunotherapy, Elife 9 (2020).

[14] M.E. Fiori, S. Di Franco, L. Villanova, P. Bianca, G. Stassi, R. De Maria, Cancer-associated fibroblasts as abettors of tumor progression at the crossroads of EMT and therapy resistance, Mol. Cancer 18 (1) (2019) 70.

[15] Z. Yu, Y. Lv, C. Su, W. Lu, R. Zhang, J. Li, B. Guo, H. Yan, D. Liu, Z. Yang, et al., Integrative single-cell analysis reveals transcriptional and epigenetic regulatory features of clear cell renal cell carcinoma, Cancer Res. 83 (5) (2023) 700–719.

[16] M. Meylan, F. Petitprez, E. Becht, A. Bougoüin, G. Pupier, A. Calvez, I. Giglioli, V. Verkarre, G. Lacroix, J. Verneau, et al., Tertiary lymphoid structures generate and propagate anti-tumor antibody-producing plasma cells in renal cell cancer, Immunity 55 (3) (2022) 527–541.e525.

[17] V. Thorsson, D.L. Gibbs, S.D. Brown, D. Wolf, D.S. Bortone, T.H. Ou Yang, E. Porta-Pardo, G.F. Gao, C.L. Plaisier, J.A. Eddy, et al., The immune landscape of cancer, Immunity 51 (2) (2019) 411–412.

[18] M.E. Ritchie, B. Phipson, D. Wu, Y. Hu, C.W. Law, W. Shi, G.K. Smyth, Limma powers differential expression analyses for RNA-sequencing and microarray studies, Nucleic Acids Res. 43 (7) (2015) e47.

[19] V. Svetnik, A. Liaw, C. Tong, J.C. Culberson, R.P. Sheridan, B.P. Feuston, Random forest: a classification and regression tool for compound classification and QSAR modeling, J. Chem. Inf. Comput. Sci. 43 (6) (2003) 1947–1958.

[20] J. Friedman, T. Hastie, R. Tibshirani, Regularization paths for generalized linear models via coordinate descent, J. Stat. Software 33 (1) (2010) 1–22.

[21] N. Simon, J. Friedman, T. Hastie, R. Tibshirani, Regularization paths for cox's proportional hazards model via coordinate descent, J. Stat. Software 39 (5) (2011) 1–13.

[22] J.K. Tay, B. Narasimhan, T. Hastie, Elastic net regularization paths for all generalized linear models, J. Stat. Software 106 (2023).

[23] D. Zeng, Z. Ye, R. Shen, G. Yu, J. Wu, Y. Xiong, R. Zhou, W. Qiu, N. Huang, L. Sun, et al., IOBR: multi-omics immuno-oncology biological research to decode tumor microenvironment and signatures, Front. Immunol. 12 (2021) 687975.

[24] R. Satija, J.A. Farrell, D. Gennert, A.F. Schier, A. Regev, Spatial reconstruction of single-cell gene expression data, Nat. Biotechnol. 33 (5) (2015) 495–502.

[25] E.Z. Macosko, A. Basu, R. Satija, J. Nemesh, K. Shekhar, M. Goldman, I. Tirosh, A.R. Bialas, N. Kamitaki, E.M. Martersteck, et al., Highly parallel genome-wide expression profiling of individual cells using nanoliter droplets, Cell 161 (5) (2015) 1202–1214.

[26] Y. Hao, S. Hao, E. Andersen-Nissen, W.M. Mauck 3rd, S. Zheng, A. Butler, M.J. Lee, A.J. Wilk, C. Darby, M. Zager, et al., Integrated analysis of multimodal single-cell data, Cell 184 (13) (2021) 3573–3587.e3529.

[27] T. Stuart, A. Butler, P. Hoffman, C. Hafemeister, E. Papalexi, W.M. Mauck, Y. Hao, M. Stoeckius, P. Smibert, R. Satija, Comprehensive integration of single-cell data, Cell 177 (7) (2019) 1888–1902.e1821.

[28] S. Hänzelmann, R. Castelo, J. Guinney, GSVA: gene set variation analysis for microarray and RNA-seq data, BMC Bioinf. 14 (2013) 7.

[29] Ø. Borgan, in: Terry M. Therneau, Patricia M. Grambsch (Eds.), Modeling Survival Data: Extending the Cox Model, Springer-Verlag, New York, 2000, pp. 2053–2054. **No. of pages: xiii + 350. Price: $69.95. ISBN 0-387-98784-3**. 2001, **20**(13).

[30] A. Jalali, A. Alvarez-Iglesias, D. Roshan, J. Newell, Visualising statistical models using dynamic nomograms, PLoS One 14 (11) (2019) e0225253.

[31] H. Wickham, ggplot2: Elegant Graphics for Data Analysis, Springer Cham, 2016.

[32] L. Zhang, X. Yu, L. Zheng, Y. Zhang, Y. Li, Q. Fang, R. Gao, B. Kang, Q. Zhang, J.Y. Huang, et al., Lineage tracking reveals dynamic relationships of T cells in colorectal cancer, Nature 564 (7735) (2018) 268–272.

[33] R. Moncada, D. Barkley, F. Wagner, M. Chiodin, J.C. Devlin, M. Baron, C.H. Hajdu, D.M. Simeone, I. Yanai, Integrating microarray-based spatial transcriptomics and single-cell RNA-seq reveals tissue architecture in pancreatic ductal adenocarcinomas, Nat. Biotechnol. 38 (3) (2020) 333–342.

[34] T. Stuart, A. Srivastava, S. Madad, C.A. Lareau, R. Satija, Single-cell chromatin state analysis with Signac, Nat. Methods 18 (11) (2021) 1333–1341.

[35] M. Lawrence, W. Huber, H. Pagès, P. Aboyoun, M. Carlson, R. Gentleman, M.T. Morgan, V.J. Carey, Software for computing and annotating genomic ranges, PLoS Comput. Biol. 9 (8) (2013) e1003118.

[36] G. Yu, L.G. Wang, Q.Y. He, ChIPseeker: an R/Bioconductor package for ChIP peak annotation, comparison and visualization, Bioinformatics 31 (14) (2015) 2382–2383.

[37] C. Trapnell, D. Cacchiarelli, J. Grimsby, P. Pokharel, S. Li, M. Morse, N.J. Lennon, K.J. Livak, T.S. Mikkelsen, J.L. Rinn, The dynamics and regulators of cell fate decisions are revealed by pseudotemporal ordering of single cells, Nat. Biotechnol. 32 (4) (2014) 381–386.

[38] X. Qiu, A. Hill, J. Packer, D. Lin, Y.A. Ma, C. Trapnell, Single-cell mRNA quantification and differential analysis with Census, Nat. Methods 14 (3) (2017) 309–315.

[39] Q. Liu, C.Y. Hsu, Y. Shyr, Scalable and model-free detection of spatial patterns and colocalization, Genome Res. 32 (9) (2022) 1736–1745.

[40] K. Yoshihara, M. Shahmoradgoli, E. Martínez, R. Vegesna, H. Kim, W. Torres-Garcia, V. Treviño, H. Shen, P.W. Laird, D.A. Levine, et al., Inferring tumour purity and stromal and immune cell admixture from expression data, Nat. Commun. 4 (1) (2013) 2612.

[41] T. Wu, E. Hu, S. Xu, M. Chen, P. Guo, Z. Dai, T. Feng, L. Zhou, W. Tang, L. Zhan, et al., clusterProfiler 4.0: a universal enrichment tool for interpreting omics data, Innovation 2 (3) (2021) 100141.

[42] G. Yu, L.G. Wang, Y. Han, Q.Y. He, clusterProfiler: an R package for comparing biological themes among gene clusters, OMICS 16 (5) (2012) 284–287.

[43] I. Dolgalev, MSigDB Gene Sets for Multiple Organisms in a Tidy Data Format **[R Package Msigdbr Version 7.4.1]**, 2021, 2021.

[44] R. Moncada, D. Barkley, F. Wagner, M. Chiodin, J.C. Devlin, M. Baron, C.H. Hajdu, D.M. Simeone, I. Yanai, Integrating microarray-based spatial transcriptomics and single-cell RNA-seq reveals tissue architecture in pancreatic ductal adenocarcinomas, Nat. Biotechnol. 38 (3) (2020) 333–342.

[45] B. Schoeps, J. Frädrich, A. Krüger, Cut loose TIMP-1: an emerging cytokine in inflammation, Trends Cell Biol. 33 (5) (2023) 413–426.

[46] H.I. Wettersten, O.A. Aboud, P.N. Lara Jr., R.H. Weiss, Metabolic reprogramming in clear cell renal cell carcinoma, Nat. Rev. Nephrol. 13 (7) (2017) 410–419.

[47] P.P. Kapitsinou, V.H. Haase, The VHL tumor suppressor and HIF: insights from genetic studies in mice, Cell Death Differ. 15 (4) (2008) 650–659.

[48] L. Sun, H. Zhang, P. Gao, Metabolic reprogramming and epigenetic modifications on the path to cancer, Protein Cell 13 (12) (2022) 877–919.

[49] R. Hoefflin, S. Harlander, S. Schäfer, P. Metzger, F. Kuo, D. Schönenberger, M. Adlesic, A. Peighambari, P. Seidel, C.Y. Chen, et al., HIF-1α and HIF-2α differently regulate tumour development and inflammation of clear cell renal cell carcinoma in mice, Nat. Commun. 11 (1) (2020) 4111.

[50] M. Certo, C.H. Tsai, V. Pucino, P.C. Ho, C. Mauro, Lactate modulation of immune responses in inflammatory versus tumour microenvironments, Nat. Rev. Immunol. 21 (3) (2021) 151–161.

[51] L. Xia, L. Oyang, J. Lin, S. Tan, Y. Han, N. Wu, P. Yi, L. Tang, Q. Pan, S. Rao, et al., The cancer metabolic reprogramming and immune response, Mol. Cancer 20 (1) (2021) 28.

[52] M. Jin, W. Cao, B. Chen, M. Xiong, G. Cao, Tumor-derived lactate creates a favorable niche for tumor via supplying energy source for tumor and modulating the tumor microenvironment, Front. Cell Dev. Biol. 10 (2022) 808859.

[53] L. Chen, L. Huang, Y. Gu, W. Cang, P. Sun, Y. Xiang, Lactate-lactylation hands between metabolic reprogramming and immunosuppression, Int. J. Mol. Sci. 23 (19) (2022).

[54] Y. Chen, K.M. McAndrews, R. Kalluri, Clinical and therapeutic relevance of cancer-associated fibroblasts, Nat. Rev. Clin. Oncol. 18 (12) (2021) 792–804.

[55] Z. Yang, C. Yan, J. Ma, P. Peng, X. Ren, S. Cai, X. Shen, Y. Wu, S. Zhang, X. Wang, et al., Lactylome analysis suggests lactylation-dependent mechanisms of metabolic adaptation in hepatocellular carcinoma, Nat. Metab. 5 (1) (2023) 61–79.

[56] Y. Shou, Y. Liu, J. Xu, J. Liu, T. Xu, J. Tong, L. Liu, Y. Hou, D. Liu, H. Yang, et al., TIMP1 indicates poor prognosis of renal cell carcinoma and accelerates tumorigenesis via EMT signaling pathway, Front. Genet. 13 (2022) 648134.

[57] P. Duch, N. Díaz-Valdivia, R. Ikemori, M. Gabasa, E.S. Radisky, M. Arshakyan, S. Gea-Sorlí, A. Mateu-Bosch, P. Bragado, J.L. Carrasco, et al., Aberrant TIMP-1 overexpression in tumor-associated fibroblasts drives tumor progression through CD63 in lung adenocarcinoma, Matrix Biol. : journal of the International Society for Matrix Biology 111 (2022) 207–225.